Biosynthesized spinel Ce-NiFe$_2$O$_4$ nanoparticles by *Pedalium murex* extract assisted combustion method: Antibacterial, photocatalytic and magneto-optical properties

K. Thanrasu [1,*]**, A. Dinesh** [1]**, K. Kanmani Raja** [1,*]

[1] Department of Chemistry, Government Arts College for Men (Autonomous), Affiliated to the University of Madras, Nandanam, Chennai – 600035, Tamil Nadu, India

*Corresponding Author Email addresses: kthanrasut@gmail.com (K. Thanrasu); kkanmaniraja@gmail.com (K. Kanmani Raja)

Abstract

Nanocrystalline NiCe$_x$Fe$_{2-x}$O$_4$ (x = 0, 0.2, 0.4 and 0.6) magnetic spinel materials were synthesized by a simple microwave combustion technique (MCT) by utilizing the fuel of *Pedalium murex* plant extract. The establishment of a cubic spinel structure was ensured by powder X-ray diffraction (PXRD) technique and the crystallites size was found to be in the range of 27.5 to 13.1 nm for NiFe$_2$O$_4$ and Ce:NiFe$_2$O$_4$ nanoparticles (NPs). The morphology of the NiFe$_2$O$_4$ NPs was observed by high resolution scanning electron microscope (HR-SEM). Energy dispersive X-ray (EDX) studies confirmed the formation of pure spinel ferrite structure as they ensured the presence of all the elements and the formation of the desired compositions. Furthermore, the bandgap value was estimated to be within 3.26 and 3.39 eV. The appearance of

Fourier transform infrared (FT-IR) bonds at 437 and 456 cm^{-1} is linked to the octahedral (B) metal stretching (Ni-O) and the band at 582 cm^{-1} is linked to the tetrahedral (A) metal stretching (Fe-O), which ensure the formation of cerium substituted $NiFe_2O_4$ NPs. Magnetic parameters such as remanent magnetization (M_r), coercivity (H_c) and saturation magnetization (M_s) were calculated from M-H loops, which exhibited ferromagnetic behaviour. The photocatalytic (PC) behavior of $NiFe_2O_4$, $NiCe_{0.2}Fe_{1.8}O_4$, $NiCe_{0.4}Fe_{1.6}O_4$ and $NiCe_{0.6}Fe_{1.4}O_4$ were analyzed under visible light irradiation by the degradation (PCD) of an aqueous solution of Rhodamine B (RhB) dye. Among the various prepared compositions, $NiCe_{0.4}Fe_{1.6}O_4$ exhibits higher PCD efficiency as 93.88 % at 120 min with enhanced visible light absorption range. The antibacterial activities of gram-positive *Staphylococcus aureus*, *Bacillus subtilis and* gram-negative *Escherichia coli* and *Klebsiella pneumonia* have been investigated using pure and Ce^{3+} substituted $NiFe_2O_4$ NPs. It was found that the improved activity is intensified with smooth Ce^{3+} doping as it cause a decrease in the grain size.

Keywords: Antibacterial activity; Ce substituted $NiFe_2O_4$ NPs; *Pedalium murex* plant extract; Optical properties; Magnetic properties; Photocatalyst.

1. Introduction

In recent years, semiconducting materials have gained much attention in the field of nanoscience and nanotechnology, because of their exceptional optical, electrical, structural, and magnetic characteristics. Metal oxides are widely used in various applications such as in magnetic storage and energy storage device, piezoelectric devices, resistive memory devices, photocatalytic degradation, etc. [1-4]. The cubic spinel structure has a general formula of AB_2O_4 where divalent

metal ions $A^{2+}= Co^{2+}, Zn^{2+}, Mn^{2+}, Ni^{2+}$, etc occupy the tetrahedral (A) sites, and trivalent metal ions $B^{3+}= Fe^{3+}, Al^{3+}$, etc. occupy the octahedral (B) sites [6]. It is observed that these ferrites exhibited distinct magnetic and physical characteristics upon the alteration of the divalent cations.

By altering the divalent cations, it is feasible to obtain expressively different magnetic and physical characteristics in ferrites. The previous studies convey that Ce-Ni ferrites exhibit unique characteristics and proved to be versatile magnetic materials widely used in microwave devices, power transformers, read and or write heads for extraordinary speediness digital tape power transformers, rod antennas, and gas sensing material [5-7]. $Ce:NiFe_2O_4$ NPs portray mixed spinel structure where Ce^{3+}, Ni^{2+}, and Fe^{3+} ions reside in the octahedral (B) sites, while Ce^{3+}, Ni^{2+}, and Fe^{3+} ions reside in the tetrahedral (A) sites of the lattice [8]. When the ferrites are prepared at lower temperatures and the corresponding particle size lies in the nano regime, a difference in the distribution of several ions in the A- and B- sites will be happened [9, 10].

The techniques such as sol-gel, solvothermal, microwave-assisted combustion method, co-precipitation, ball milling method, and hydrothermal are widely used to synthesize cerium substituted nickel ferrite nanoparticles [11-15]. However, the above-stated approaches are found to be costly, tough to synthesis, high budget, time overwhelming and profit was low. In addition, microwave combustion technique (MCT) is used to synthesize Ce substituted $NiFe_2O_4$ NPs by this report. In this technique, there is a sudden escalation in the temperature of the precursor, due to the fundamental nature of microwave energy (ME), which produces heat and conversion by the asset of its robust intermolecular friction.

Precursors of metal nitrates and the fuel *Pedalium murex* plant extract in a suitable stoichiometric ratio encourage the exothermic and self-sustaining reaction by the combustion process as per the propellant chemistry principle. The suitable plant extract fuels are usually *Aloe vera*, *Sesamum indicum*, *Hibiscus rosa-sinensis*, *Abelmoschus esculentus*, *Pedalium Murex,* and *Opuntia dillenii* [16-23]. With alteration in the cerium content, a high disparity in the characteristics viz. structural, morphological, magneto-optical, vibrational, and photocatalytic properties will be observed. In this paper, $NiCe_xFe_{2-x}O_4$ (x = 0, 0.2, 0.4 and 0.6) NPs were synthesized through MCT technique and be utilizing the fuel extracted from *Pedalium murex* plant. The phase, morphological, vibrational, optical, antibacterial activity, magnetic, and photocatalytic characteristics are studied using various physical characterization techniques.

2. Experimental

2.1. Synthesis

Spinel $NiCe_xFe_{2-x}O_4$ nanoparticles were synthesized using the corresponding metal nitrates $Ni(NO_3)_2 \cdot 6H_2O$, $Ce(NO_3)_3 \cdot 6H_2O$, $Fe(NO_3)_3 \cdot 9H_2O$, and the fuel plant extracted from *Pedalium murex*. The chemicals were brought from SD fine (India) that were of analytical grade and utilized as received. To prepare the desired compositions, the precursors of $Ni(NO_3)_2 \cdot 6H_2O$, $Ce(NO_3)_3 \cdot 6H_2O$ and $Fe(NO_3)_3 \cdot 9H_2O$ were mixed by maintaining a molar ratio of 1:2 and dissolved in double distilled water. Plant extracts of *Pedalium murex* solution was added to the main achieved solutions and stirred for 1 hour. Here, plant extracts of *Pedalium murex* work as fuel, whereas the precursors of metal nitrates function as oxidizers.

The final obtained homogeneous solutions were transported into silica crucibles and were located in microwave ovens (attained from SAMSUNG, India) utilized for the mechanism of irradiation (**Scheme 1**). The yield power was set as 900 Watts for 10 min and the frequency was maintained at 2.54 GHz. Under the influence of ME, the solutions subjected to the procedures like boiling, vaporization, dehydration, and finally decomposition, that result in the evolution of reaction gas.

When the solutions attained impulsive combustion, the explosion took place, which causes rapid flame fluffy production of pure and Ce substituted $NiFe_2O_4$. Furthermore, the obtained samples were washed with distilled (DI) water, ethanol, and then dried at 550 °C for 150 min. The obtained powder products viz. x = 0, 0.2, 0.4 and 0.6 were labeled as $NiFe_2O_4$, $NiCe_{0.2}Fe_{1.8}O_4$, $NiCe_{0.4}Fe_{1.6}O_4$ and $NiCe_{0.6}Fe_{1.4}O_4$, respectively.
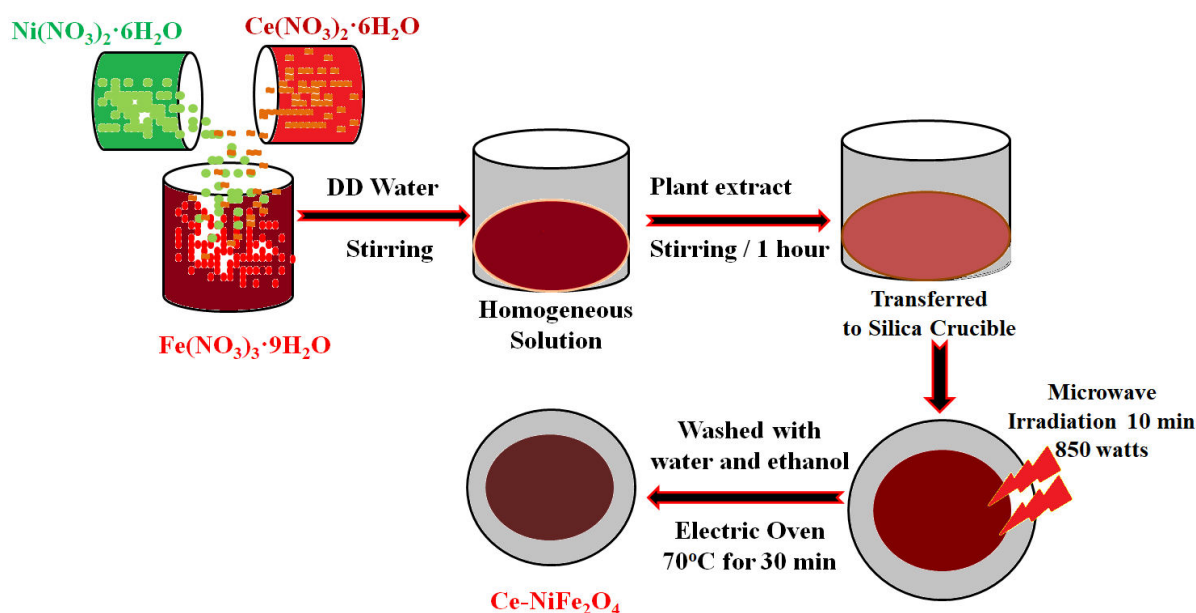
Scheme 1. Schematic representation of synthesis of spinel $NiCe_xFe_{2-x}O_4$ ($0 \leq x \leq 0.6$)

nanoparticles.

2.2. Characterization techniques

Powder X-ray diffractometer (Model Rigaku Ultima III)is employed to confirm the formation of different phases and investigate the crystal structure of the obtained Ce-substituted $NiFe_2O_4$ nanoparticles by employing CuKα radiation (λ = 1.5406 Å) and within 2θ range of 20° - 80°. FEI Quanta FEG 200 scanning electron microscope accompanied by energy dispersive X-ray analyzer is utilized to perform the morphological and elemental analysis. The diffuse reflectance spectra were logged in the range of 200-800 nm by utilizing Perkin Elmer (Thermo Scientific Evolution 220) spectrophotometer from which the bandgap value is deduced. Perkin Elmer spectrophotometer (Spectrum RX1) is utilized to log the FTIR spectra. Lake Shore (Model7404, USA,) vibration sample magnetometer (VSM) equipped with 3 magnets is used to perform magnetization measurements at RT.

2.3 Photocatalytic evaluation

The photocatalytic performance of $NiFe_2O_4$, $NiCe_{0.2}Fe_{1.8}O_4$, $NiCe_{0.4}Fe_{1.6}O_4$ and $NiCe_{0.6}Fe_{1.4}O_4$ nanoparticles were examined under visible light (300 W Xenon lamps; λ >400 nm) irradiation. The photocatalytic activity of the as-prepared samples was analyzed at room temperature. Exactly 100 mg of photocatalyst was dispersed in 100 mL of Rhodamine B (RhB) (10 mg/L), which was reserved in a quartz glass photocatalytic reactor. Before irradiation, the aliquot was stirred 30 min in a dark condition and ensured that the catalyst adsorption-desorption equilibrium was attained between the dye and the photocatalyst. The degradation efficiency was examined

using UV absorption studies, which lead to determine the dye concentrations at a certain time interval. The catalytic performance of the pure $NiFe_2O_4$ and cerium doped $NiFe_2O_4$ at various percentages was also investigated.

2.3. Antibacterial activity

The antibacterial activity (ABA) of spinel $NiFe_2O_4$, $NiCe_{0.2}Fe_{1.8}O_4$, $NiCe_{0.4}Fe_{1.6}O_4$ and $NiCe_{0.6}Fe_{1.4}O_4$ NPs was analyzed by their zone of inhibitions on the human pathogens (HP) gram-positive *S. aureus (Staphylococcus aureus)*, *B. subtilis* (*Bacillus subtilis*) *and* gram-negative *E. coli (Escherichia coli)* and *K. pneumonia (Klebsiella pneumoniae)* . An instant culture of all microorganisms was attuned to an OD of 0.1 and wiped onto Mueller Hilton (MH) agar plates. By a cork borer (CB), holes were stamped on the agar, followed by adding of the standard solutions containing the synthesized $NiFe_2O_4$, $NiCe_{0.2}Fe_{1.8}O_4$, $NiCe_{0.4}Fe_{1.6}O_4$ and $NiCe_{0.6}Fe_{1.4}O_4$ NPs (10µg/mL). The plates were incubated at 37˚C for 24 h and the precinct of inhibitions on the human pathogens was dignified in diameter.

3. Results and discussion

3.1. Phase analysis

XRD patterns of the as-prepared spinel $NiFe_2O_4$ and $Ce:NiFe_2O_4$ NPs are illustrated in **Fig. 1.** From the attained powder patterns it is confirmed that the prepared samples were polycrystalline. The peaks at 2θ values of 18.24˚, 30.13˚, 35.51˚, 37.20˚, 43.23˚, 54.03˚, 57.26˚, 62.92˚ and 75.35˚ are mapped to (111), (220), (311), (222), (400), (422), (511), (440) and (622) reflection planes of $NiFe_2O_4$, respectively. The attained diffraction peaks go with diffraction data (JCPDS

card number 44-1485), ensuring the establishment of spinel cubic structure with *Fd-3m* space group [24]. The observed impurity peaks were associated to the α-Fe_2O_3 phase verified by the card ICSD – 088418 data. This contamination phase may be due to the oxidation ability of Ni^{2+} ion and the combustion in oxygen-rich environment [25].

The crystallite (*L*) of the obtained samples estimated using (311) hkl plane by retaining Debye Scherrer's Eq. (1).

$$L = \frac{0.89\lambda}{\beta \cos\theta} \qquad (1)$$

Where, *L*, average crystallite size, λ, X-ray source wavelength (0.15406 nm), β, FWHM (full width at half maximum) of the peak; and θ, diffraction angle. The value of the crystallites size deduced for $NiFe_2O_4$ and $Ce:NiFe_2O_4$ NPs, consistent with the diffraction peak (311), were established to be within the interval 27.52 to 13.12 nm (**Table 1**).

To deduce the lattice parameter of the $NiFe_2O_4$ and $Ce:NiFe_2O_4$ NPs, Eq. 2 was used.

$$a = d_{hkl}\sqrt{(h^2 + k^2 + l^2)} \qquad (2)$$

Where, d_{hkl}, the inter-atomic spacing consistent to the Miller indices h, k, and l of the crystal planes and *a,* is the lattice parameter. **Fig. 2** shows that the lattice parameter '*a*' resembles the cubic spinel structure. The lattice parameter '*a*' value was calculated for $NiFe_2O_4$ and $Ce:NiFe_2O_4$ NPs and it was found to be 8.332 Å and 8.389 Å respectively, which was traced to be in line with the formerly stated value of 8.337 Å [26]. This increase of '*a*' is due to the replacement of larger ionic size Ce cations (0.92 Å) in place of the lower ionic size Fe cations (0.67 Å) [3]. The Ce^{3+} ion ionic radius larger and as it takes the place of Fe^{3+} ions, resulting in a slight expansion of the crystal size, which was observed to be in line with Vegard's law.

The effective size of the particle (D) is obtained by employing Williamson-Hall (W-H) plot equation:

$$\frac{\beta \cos \theta}{\lambda} = \frac{k}{D} + \frac{4\varepsilon \sin \theta}{\lambda} \qquad (3)$$

0.89 is the value of the constant *k*. and the strain associated with samples represented by ε. **Fig. 3** shows the W-H plot (i.e. $4\sin\theta/\lambda$ versus $\beta\cos\theta/\lambda$) where the interrupt (k/D) is used to control the actual particle size (D).

W-H plot for $NiFe_2O_4$ and $Ce:NiFe_2O_4$ NPs is represented in **Fig. 3** and observed that the crystallite size attained by W-H method is lesser in comparison with crystallite size deduced by Debye Scherer's method. The variance is chiefly due to the participation of the strain module in the W-H method. It is perceived that with an increase in Ce content (*x*), the crystallite size shrinkages, whereas an escalation in the lattice parameter was observed [27].
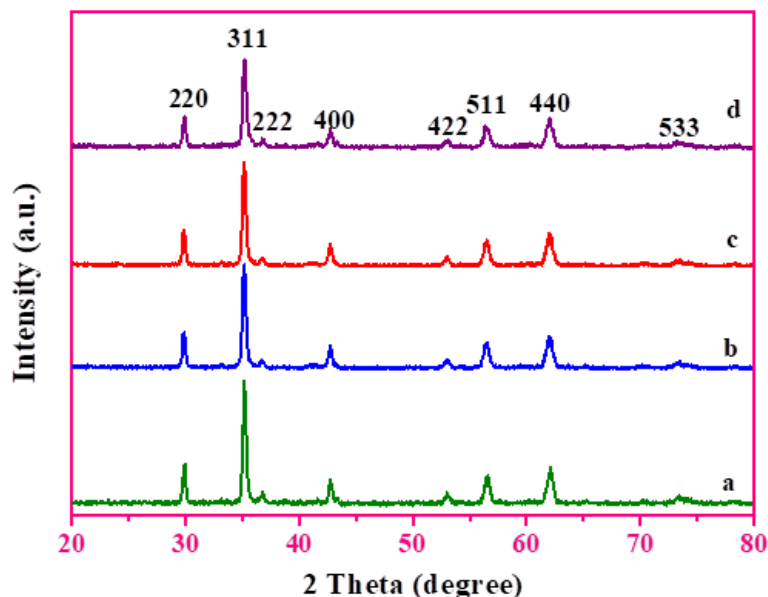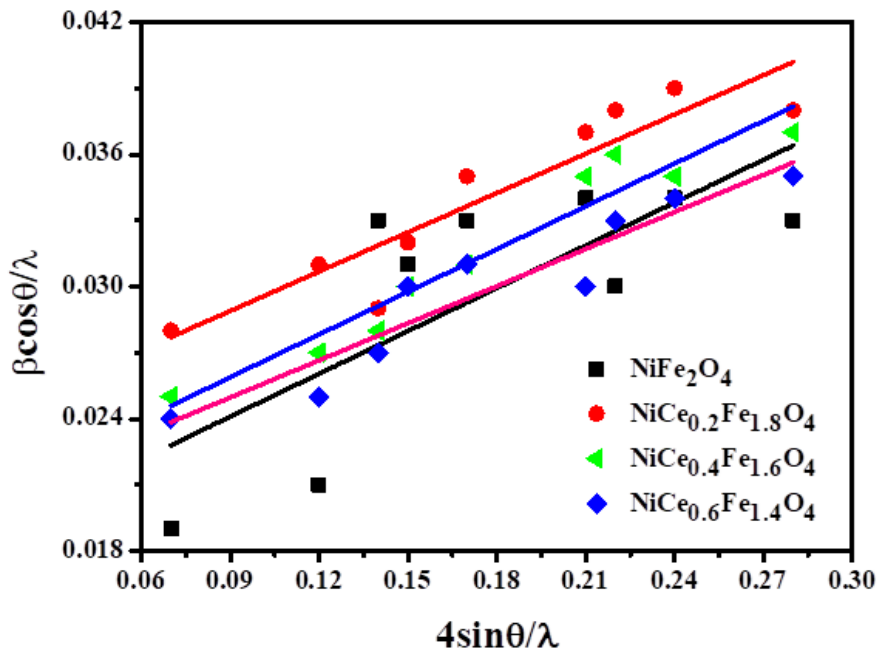
Figure 1. XRD patterns of spinel $NiCe_xFe_{2-x}O_4$ $(0 \leq x \leq 0.6)$ nanoparticles.
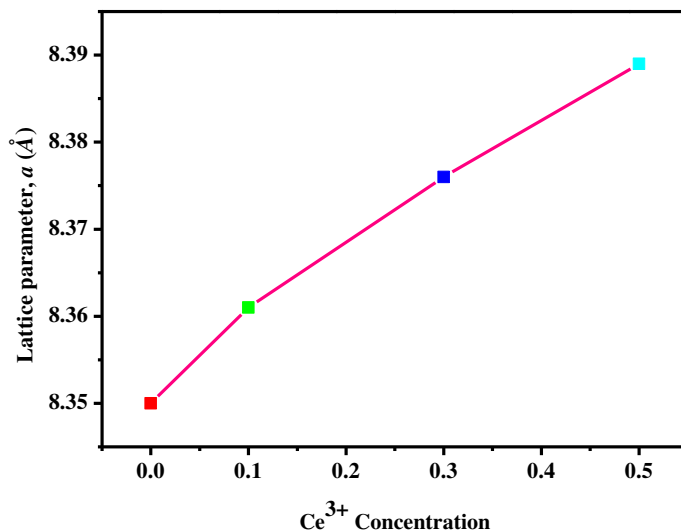
Figure 2. Variation of lattice constant of spinel $NiCe_xFe_{2-x}O_4$ $(0 \leq x \leq 0.6)$ nanoparticles.

Table 1. **Crystallite size (L) and lattice parameter (a) and energy gap (Eg) of spinel $NiCe_xFe_{2-x}O_4$ $(0 \leq x \leq 0.6)$ nanoparticles.**

Sample Name	Crystallite Size, L (nm)	Effective crystallite size, D (nm) by William-Hall plot	Lattice Parameter, a (Å)	Energy gap, E_g (eV)
$NiFe_2O_4$	27.52	28.48	8.350	3.39
$NiCe_{0.2}Fe_{1.8}O_4$	24.31	23.31	8.361	3.36
$NiCe_{0.4}Fe_{1.6}O_4$	13.28	12.95	8.376	3.30
$NiCe_{0.6}Fe_{1.4}O_4$	19.12	18.10	8.389	3.26

Figure 3. W-H patterns of spinel $NiCe_xFe_{2-x}O_4$ ($0 \leq x \leq 0.6$) nanoparticles.

3.2 SEM analysis

$NiFe_2O_4$ and $Ce:NiFe_2O_4$ NPs morphology study was performed with the aid of HR-SEM. The obtained SEM images of $NiFe_2O_4$ NPs illustrated a spherical morphology and also reveal coalescence and agglomerated grains as shown in **Fig. 4**. The agglomerated and spherical morphology was noticed in the $NiCe_xFe_{2-x}O_4$ ($x = 0$ to 0.6) NPs, which is mainly due to the lower ME release during the progression of combustion [28].
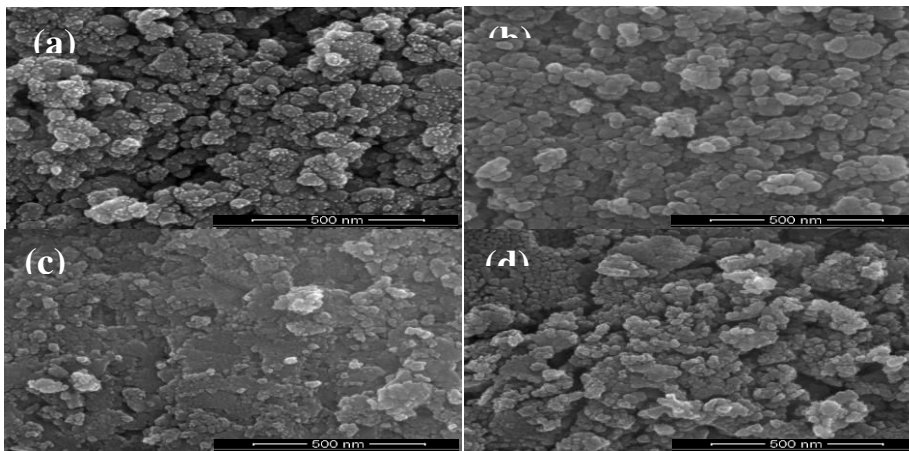
Figure 4. HR-SEM images of (a) $NiFe_2O_4$, (b) $NiCe_{0.2}Fe_{1.8}O_4$, (c) $NiCe_{0.4}Fe_{1.6}O_4$ and (d) $NiCe_{0.6}Fe_{1.4}O_4$ samples.

3.3 HR-TEM analysis

To find further evidence on the nano-scaled fine structure of $NiCe_xFe_{2-x}O_4$ (x = 0.0, 0.2 to 0.6) NPs, a structural analysis was performed by high resolution transmission electron microscopy (HR-TEM) and is revealed in **Fig. 5a-c**, respectively. The HR-TEM images of the samples clearly show that spherical shaped particles like nanostructures. Crystallographic clarifications of the as-prepared sample were done by recording the SAED (selected area electron diffraction) patterns of $NiCe_xFe_{2-x}O_4$ (x = 0.4) NPs as shown in **Fig. 5d**. A set of significant Debye rings agreeing to *hkl* planes; 311, 400, 511, and 440 of $NiFe_2O_4$ cubic crystal structure indexed a test of the purity and crystallinity of the products. The Debye rings appeared as incessant and are diffused and also evidently visible, agreement to good crystallinity, which additional leaflets that the products are very much in the nano regime and well-developed nanoparticles
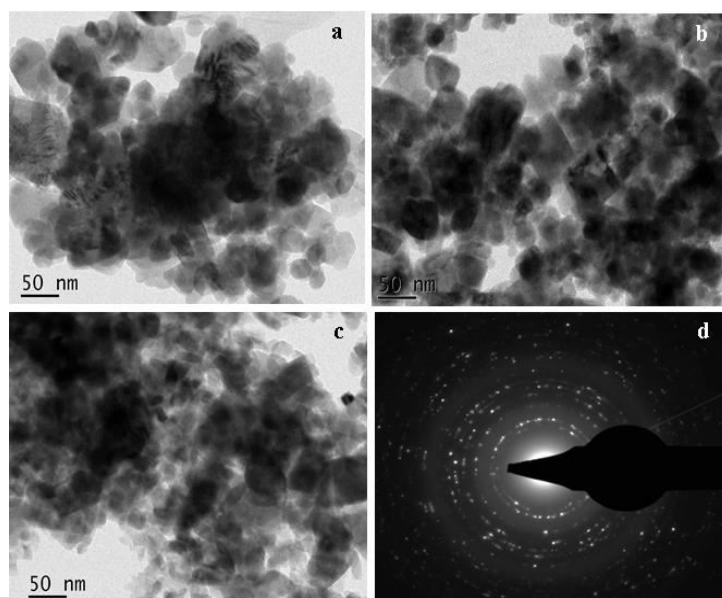
Figure 5. HR-TEM images of (a) $NiFe_2O_4$, (b) $NiCe_{0.2}Fe_{1.8}O_4$, (c) $NiCe_{0.6}Fe_{1.4}O_4$ and (d) SAED patterns of $NiCe_{0.6}Fe_{1.4}O_4$ NPs.

3.4. Optical band gap analysis

To study the optical and bandgap features of $NiFe_2O_4$ and $Ce:NiFe_2O_4$ NPs UV-Vis DRS (diffuse reflectance spectroscopy) is used, which determined bandgap with aid of Tauc relation. Kubelka–Munk (K-M) function F(R) is utilized to transform the diffused reflectance into absorption co-efficient, as stated in equation (4).

$$\alpha = F(R) = \frac{(1-R)^2}{2R} \tag{4}$$

Where, α the absorption coefficient and *R* reflectance. Therefore, the Tauc relation can be stated in equation (5),

$$F(R)hv = A(hv - E_g)^n \tag{5}$$

Where A, *v*, h, and E_g, absorption coefficient, light frequency, Plank's constant and bandgap respectively. The permitted direct and indirect transitions are denoted by n = 2 and ½., from where the values of the both direct as well as indirect bandgap are obtained.
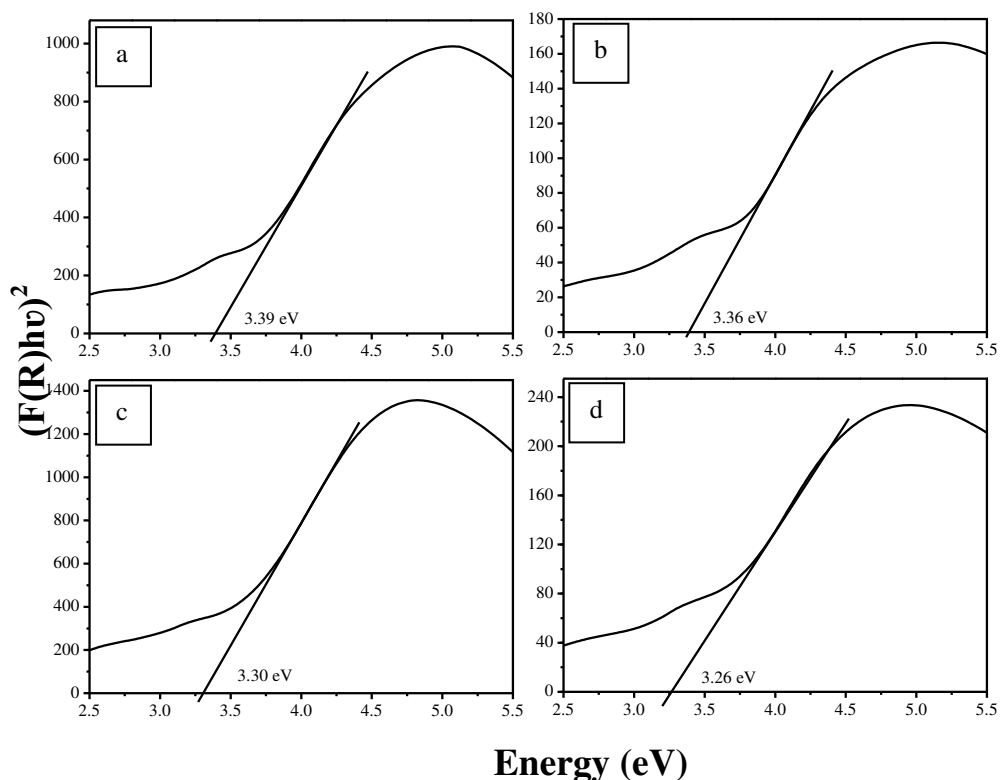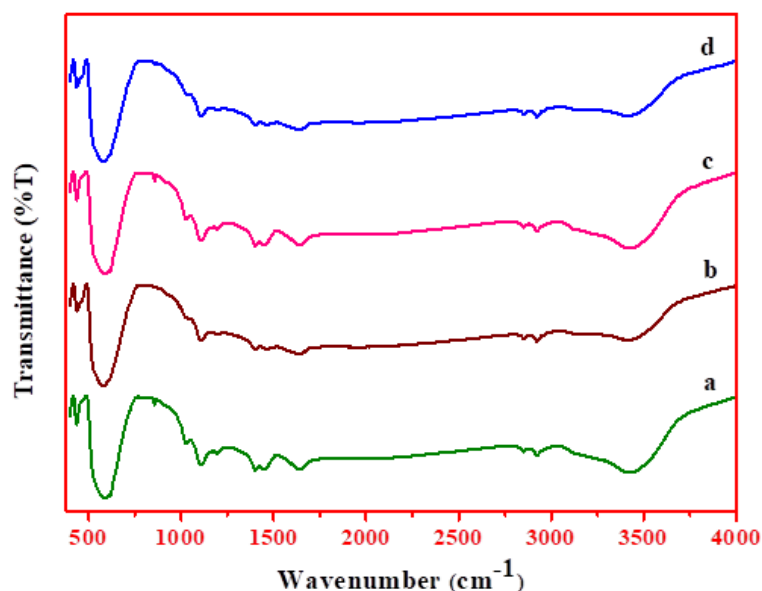
Figure 6. $(F(R)h\upsilon)^2$ versus $h\upsilon$ plots of (a) $NiFe_2O_4$, (b) $NiCe_{0.2}Fe_{1.8}O_4$, (c) $NiCe_{0.4}Fe_{1.6}O_4$ and (d) $NiCe_{0.6}Fe_{1.4}O_4$ samples.

The intention of the band-gap energy contains the extrapolation of the linear part of the curve attained by plotting $(F(R)hv)^2$ versus hv to intersect the energy axis for all compositions (**Fig. 6**). The bandgap values can be deduced by extrapolation of the direct positions in the Tauc plot $(F(R)hv)^2$ [29, 30]. The estimated energy band gap values were found to be 3.39, 3.36, 3.30 eV and 3.26 eV, whereas for the bulk $NiFe_2O_4$ bandgap material the bandgap was found to be 2.2 eV [31]. The variations of the optical bandgap due to the defects, additional sub-band energy molded by substation of Ce^{3+} ions and crystallite size of the nanoparticles [32].

3.5 FT-IR Spectral analysis

FT-IR spectra of $NiFe_2O_4$ and $Ce:NiFe_2O_4$ NPs are depicted in **Fig. 7**. The FT-IR spectra were documented in the range of 4000-400 cm^{-1} at room temperature (RT). The broadband at 3441 cm^{-1} is linked to H-O stretching [33]. The C-H stretching vibration is associated with the band at 2926 and 2851 cm^{-1} [4]. The characteristic absorption bands at 1726, 1632 and 1398 cm^{-1} are assigned to the C-O stretching band, due to the presence of traces of organic species (e.g. COO^-) on the particle surface [34]. The bands at 1013, 1107, 1116, 1201 cm^{-1} are associated with the vibrations of spinel structure of $NiFe_2O_4$ NPs [35]. The bonds at 437, 456 cm^{-1}, is consigned to octahedral (B)-metal stretching (Ni-O) and 582 cm^{-1} are linked to the tetrahedral (A) metal stretching (Fe-O) [36].

Figure 7. FTIR spectra of spinel (a) $NiFe_2O_4$, (b) $NiCe_{0.2}Fe_{1.8}O_4$, (c) $NiCe_{0.4}Fe_{1.6}O_4$ and (d) $NiCe_{0.6}Fe_{1.4}O_4$ samples.

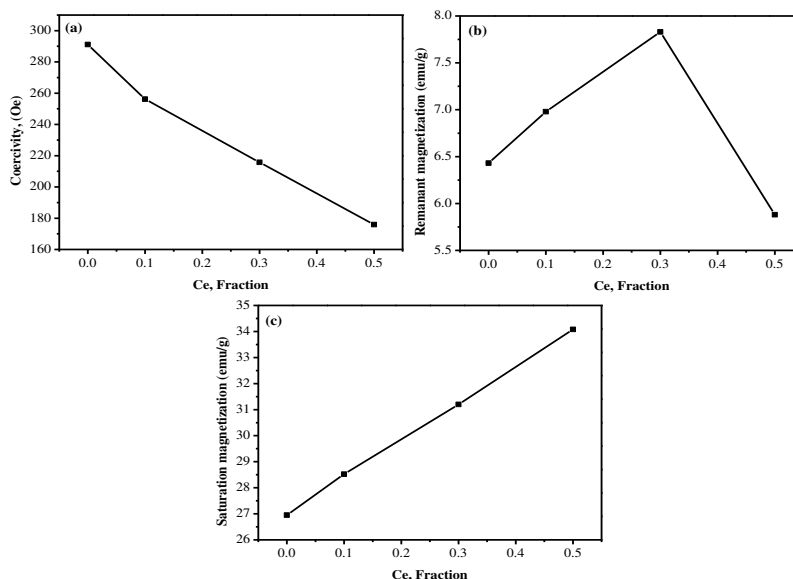*3.6. Magnetization analysis*

The magnetic parameters of $NiFe_2O_4$ and $Ce:NiFe_2O_4$ NPs were undertaken at a temperature of 300 K and a stimulated magnetic field of -15 to +15 kOe. Magnetization (M) vs. applied field (H) plots are shown in **Fig. 8.** From the hysteresis (M-H) loop, the coercivity (H_c), remanence (M_r), and saturation magnetization (M_s) were determined. $NiFe_2O_4$ and $Ce:NiFe_2O_4$ NPs exhibited normal spinel structure, as divalent (Ni^{2+}) and trivalent (Ce^{3+}/Fe^{3+}) metal ions reside in A and B sites [37-40]. The $NiFe_2O_4$ NPs were found to exhibit ferromagnetic nature. The coercivity values of $NiFe_2O_4$ and $Ce:NiFe_2O_4$ NPs were found to lie within 291.16 Oe to 175.97 Oe (**Fig. 9** and **Table 2**). The coercivity value is primarily organized by factors such as high anisotropy and cationic rearrangement [41,42]. Costa *et al.* reported superparamagnetic behavior whereas in this work ferromagnetic nature is observed. Hence, H_c values reported here are an order of magnitude smaller that those given in [5]. From the M-H hysteresis loop M_r values for $Ce:NiFe_2O_4$ NPs was found to be 6.43 emu/g (*x*= 0.0) and 7.84 emu/g (*x*= 0.3), then M_r values declined to 5.88 emu/g for (*x*= 0.5), whose values are found to be dependent on the crystallite size and shape of $NiFe_2O_4$ [8]. From the M-H loop, M_s values for $NiFe_2O_4$ and $Ce:NiFe_2O_4$ NPs were found to be within 26.95 and 34.08 emu/g.
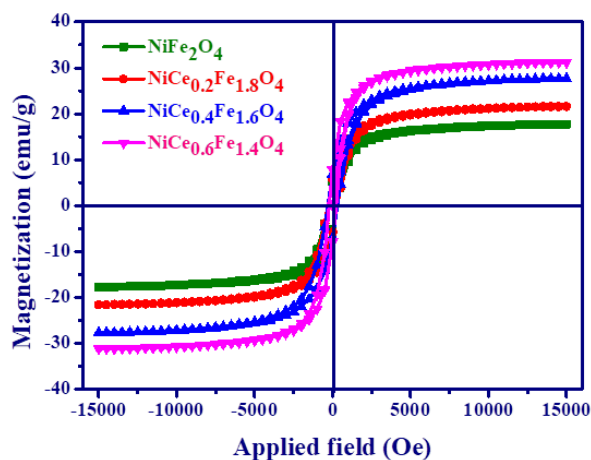
Figure 8. M-H hysteresis loops of spinel $NiCe_xFe_{2-x}O_4$ $(0 \leq x \leq 0.6)$ nanoparticles.

Sample Name	H_c, (O_e)	M_s (emu/g)	M_r (emu/g)
$NiFe_2O_4$	291.16	26.95	6.43
$NiCe_{0.2}Fe_{1.8}O_4$	256.17	28.51	6.98
$NiCe_{0.4}Fe_{1.6}O_4$	215.79	31.20	7.84
$NiCe_{0.6}Fe_{1.4}O_4$	175.97	34.08	5.88

Figure 9. Variations of (a) coercivity, (b) remanant magnetization and (c) saturation magnetization of spinel $NiCe_xFe_{2-x}O_4$ $(0 \leq x \leq 0.6)$ nanoparticles.

Table 2. Coercivity, remanant magnetization, saturation magnetization of spinel $NiCe_xFe_{2-x}O_4$ $(0 \leq x \leq 0.6)$ nanoparticles.

3.7. Photocatalytic studies

$NiFe_2O_4$ and $Ce:NiFe_2O_4$ nanoparticles were examined towards the adsorption-desorption equilibrium that was attained in 30 min and towards the photocatalytic degradation (PCD) of Rhodamine B (RhB) below visible light irradiation [43, 44]. The PCD efficiency rates of C/C_0 (%) vs. time for RhB were shown in **Fig. 10**. The photocatalytic constancy of the blank solution under visible light irradiation was calculated in the nonappearance of $NiFe_2O_4$ and $Ce:NiFe_2O_4$ NPs over 120 min, resulting in a PCD efficiency of 5.87%. The PCD efficiency of RhB solution using $NiCe_{0.4}Fe_{1.6}O_4$ NPs showed a higher degradation percentage (93.88%) than other samples. It was found that the UV-adsorption intensity of RhB decreased with the increase of the reaction time gradually. All the degradation measurement values are offered in **Table 3.**

Table 3. Percentage degradation of Rhodamine B on to Cerium doped $NiFe_2O_4$

Sample	RhB dye degradation efficiency (%)
Blank	5.87
$NiFe_2O_4$	58.31
$NiCe_{0.2}Fe_{1.8}O_4$	81.18
$NiCe_{0.4}Fe_{1.6}O_4$	93.88
$NiCe_{0.6}Fe_{1.4}O_4$	88.66
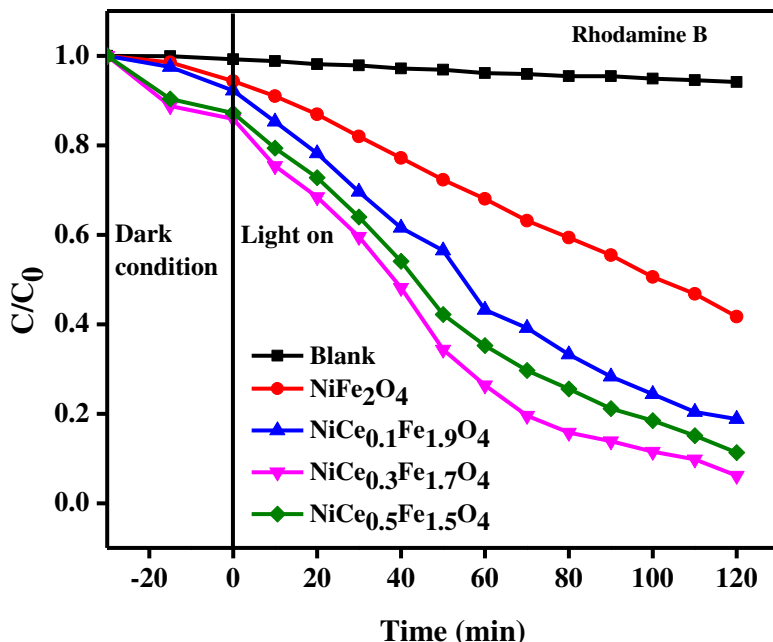
Figure 10. Rhodamine B dye degradation using spinel $NiCe_xFe_{2-x}O_4$ $(0 \leq x \leq 0.6)$ nanoparticles

3.8. Kinetic studies

The kinetics rate of RhB dye photocatalytic decomposition study of $NiFe_2O_4$ and Ce-doped $NiFe_2O_4$ catalyst surface can be signified by the -pseudo-first-order equation:.

$$-\ln(Ct/C_0) = k_{abs}(t) \tag{6}$$

Where, Ct = concentration of RhB at various time (t), C_0 = initial dye concentration and kabs = pseudo-first order rate constant of dye removal (**Fig. 11**) and noted that $NiCe_{0.3}Fe_{1.7}O_4$ possesses higher rate constant than other compositions [45, 46]. Hence, spinel $NiCe_{0.4}Fe_{1.6}O_4$ NPs is the optimal attentiveness to enhance the PCD of RhB. The rate constant k_{abs} value of RhB from the experimental data was given in **Table 4.**
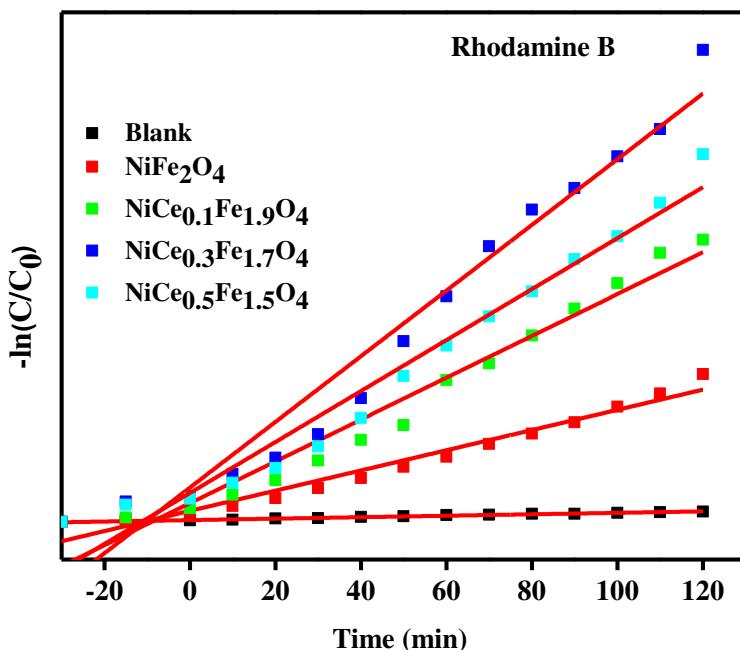
Figure 11. Pseudo first-order kinetic plot for Rhodamine B dye degradation using spinel NiCe$_x$Fe$_{2-x}$O$_4$ ($0 \leq x \leq 0.6$) nanoparticles.

Table 4. Rate constant k$_{abs}$ value for the degradation of RhB on to NiFe$_2$O$_4$

Samples	k min^{-1}				
	Blank	NiFe$_2$O$_4$	NiCe$_{0.2}$Fe$_{1.8}$O$_4$	NiCe$_{0.4}$Fe$_{1.6}$O$_4$	NiCe$_{0.6}$Fe$_{1.4}$O$_4$
RhB	0	0.006	0.0124	0.0194	0.0151

3.9. Photocatalytic degradation mechanism

Based on the above outcomes and discussions, an appropriate photocatalytic degradation mechanism for RhB degradation over Ce-doped $NiFe_2O_4$ NPs is shown in **Scheme 2**. When passing the visible light on the catalysts surface, the electrons (e⁻) get excited from VB (valence band) to CB (conduction band) of Ce-doped $NiFe_2O_4$ along with producing holes (h⁺) in the VB. The CB excited electrons of $NiFe_2O_4$ get combined Cerium and electron-hole pair recombination rates become lower, hence enhances the photocatalytic process [43-46]. The CB electron get combines with a dissolved oxygen molecule to form anions of peroxide radicals (•O_2^-) and similarly created hydroxyl radicals (•OH), owing to the reaction amongst holes and OH− ions. The RhB decomposes into a simpler molecule in the presence of •OH and •O_2^- species into CO_2 and H_2O. The appropriate PCD mechanism is listed in the equation.

$$Ce:NiFe_2O_4 + Visible\ Light\ (hv) \longrightarrow h^+(VB) + e^-\ (CB) \qquad (2)$$

$$h^+_{(VB)} + H_2O \longrightarrow H^+ + •OH \qquad (3)$$

$$e^- + O_2 \longrightarrow •O_2^- \qquad (4)$$

$$[RhB\ Dye] + •O_2^- + •OH \longrightarrow H_2O + CO_2 \qquad (5)$$
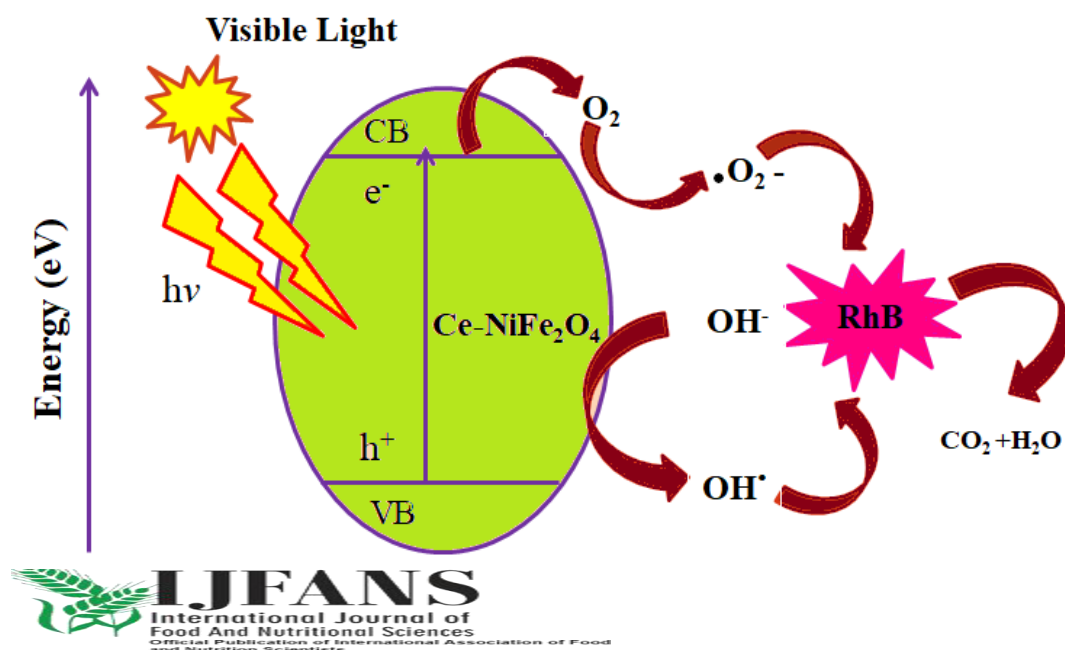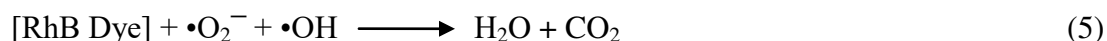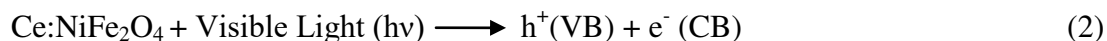
Scheme 2. Photocatalytic mechanism of Rhodamine B (RhB) dye degradation using spinel NiCe$_x$Fe$_{2-x}$O$_4$ ($0 \leq x \leq 0.6$) nanoparticles.

3.10 Antibacterial activity

The antibacterial activity of spinel NiFe$_2$O$_4$ and Ce:NiFe$_2$O$_4$ magnetic nanoparticles (**Fig. 12**) were examined beside gram-positive *S. aureus (Staphylococcus aureus)*, *B. subtilis (Bacillus subtilis) and* gram-negative *E. coli (Escherichia coli)*, *K. pneumonia (Klebsiella pneumoniae)* bacterial strains, correspondingly. From **Fig. 12**, it was originated that no zone of inhibition was obtained over the control. The variation in diameter of zone of inhibition was given in Table 5. It is found that the zone of inhibition growths with the rise in the Ce-dopant ratio [47, 48]. Moreover, a greater concentration of Ce substitution impact enhanced antibacterial activity than the lower concentration of Ce substituted NiFe$_2$O$_4$ nanopowders. The obtained smaller particle size and higher surface area with the volume ratio of the performance of the samples a vibrant character in the antibacterial activity of samples [49-52].
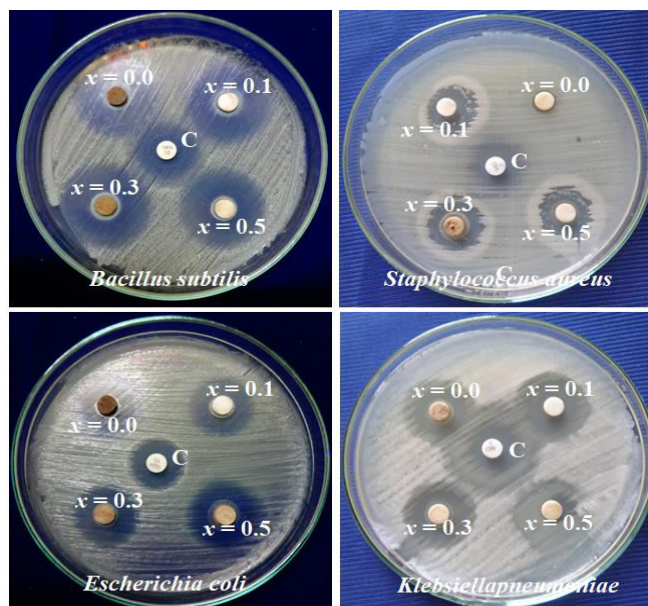
Figure. 12. Antibacterial activity of $NiCe_xFe_{2-x}O_4$ (x = 0.0, 0.2, 0.4 and 0.6) ferrite nanoparticles.

Table 5. Antibacterial activity of $NiCe_xFe_{2-x}O_4$ (x = 0.0, 0.2, 0.4 and 0.6) ferrite nanoparticles.

S. No.	Bacteria	Zone of Inhibition (mm in diameter)				
		Control	$x = 0.0$	$x = 0.2$	$x = 0.4$	$x = 0.6$
1	*Bacillus subtilis*	12	14	16	19	18
2	*Staphylococcus aureus*	10	12	14	17	16
3	*Escherichia coli*	12	10	12	16	15
4	*Klebsiellapneumoniae*	18	14	16	20	18

4. Conclusions

$NiFe_2O_4$ and $Ce:NiFe_2O_4$ samples were made by MCT and by utilizing the fuel *Pedalium murex* plant extract. XRD established the cubic spinel structure with space group *Fd-3m*. The lattice parameter (a) values were found to be in 8.350 - 8.389 Å interval. The surface morphology, structure, phase purity, and crystallinity of the samples were confirmed by HR-SEM, HR-TEM, and SAED patterns. The bandgap values were observed to lie within 3.39-3.26 eV interval attained by using the optical absorption spectra. FT-IR unveils the existence of all the characteristic functional groups of $NiFe_2O_4$ spinel nanoparticles. M_s values for $NiCe_xFe_{2-x}O_4$ nanoparticles were deduced and it is observed to lie within 26.95-34.08 emu/g respectively. It is observed that the values of M_r are strongly dependent on the crystallite size and shape. The photocatalytic degradation efficiency of Rhodamine B using $NiFe_2O_4$ and Ce doped $NiFe_2O_4$ under visible light. The photocatalyst $NiCe_{0.4}Fe_{1.6}O_4$ exhibit higher photocatalytic degradation efficiency as 93.88 % at 120 min was achieved successfully and it may apply for the environmental pollution remediation process. It was found that $Ce:NiFe_2O_4$ (x = 0.4) display

advanced antibacterial activity against *Klebsiellapneumoniae* associated with other compositions.

References

[1] M. Sertkol, Y. Koseoglu, A. Baykal, H. Kavas, A. Bozkurt, M.S. Toprak, Microwave synthesis and characterization of Zn-doped nickel ferrite nanoparticles, J. Alloys Compd. 486 (2009) 325-329.

[2] AT Ravichandran, J Srinivas, R Karthick, A Manikandan, A Baykal, Facile combustion synthesis, structural, morphological, optical and antibacterial studies of $Bi_{1-x}Al_xFeO_3$ (0.0$\leq$ x$\leq$ 0.15) nanoparticles, Ceram. Int. 44 (2018) 13247-13252.

[3] A. Kale, S. Gubbala, R.D.K. Misra, Magnetic behavior of nanocrystalline nickel ferrite synthesized by the reverse micelle technique, J. Magn. Magn. Mater. 277 (2004) 350–358.

[4] Y Slimani, A Baykal, A Manikandan, Effect of Cr^{3+} substitution on AC susceptibility of Ba hexaferrite nanoparticles, J. Magn. Magn. Mater. 458 (2018) 204-212.

[5] A.C.F.M. Costa, V.J. Silva, D.R. Cornejo, M.R. Morelli, R.H.G.A. Kiminami, L. Gama, Magnetic and structural properties of $NiFe_2O_4$ ferrite nanopowder doped with Zn^{2+}, J. Magn. Magn. Mater. 320 (2008) 370.

[6] V.D. Kapse, S.A. Ghosh, F.C. Raghuwanshi, S.D. Kapse, Nanocrystalline spinel $Ni_{0.6}Zn_{0.4}Fe_2O_4$: A novel material for H_2S sensing, Mater. Chem. Phys. 113 (2009) 638–644.

[7] V.D. Kapse, S.A. Ghosh, F.C. Raghuwanshi, S.D. Kapse, U.S. Khandekar, Nanocrystalline $Ni_{0.6}Zn_{0.4}Fe_2O_4$: A novel semiconducting material for ethanol detection, Talanta 78 (2009) 19–25.

[8] H. Kavas, A. Baykal, M.S. Toprak, Y. Koseoglu, M. Sertkol, B. Aktas, Cation distribution and magnetic properties of Zn doped $NiFe_2O_4$ nanoparticles synthesized by PEG-assisted hydrothermal route, J. Alloys Compd. 479 (2009) 49–55.

[9] J.P. Chen, C.M. Sorenson, K.J. Klabunde, G.C. Hadjipanayis, E. Devlin, A. Kostikas, Size-dependent magnetic properties of $MnFe_2O_4$ fine particles synthesized by coprecipitation, Phys. Rev. B 54 (1996) 9288–9296.

[10] A. Manikandan, S. Arul Antony, R. Sridhar, Seeram Ramakrishna, M. Bououdina, A simple combustion synthesis and optical studies of magnetic $Zn_{1-x}Ni_xFe_2O_4$ nanostructures for photoelectrochemical applications, J. Nanosci. Nanotechnol. 15 (2015) 4948-4960.

[11] M. Srivastava, S. Chaubey, Animesh K. Ojha, Investigation on size dependent structural and magnetic behavior of nickel ferrite nanoparticles prepared by sol-gel and hydrothermal methods, Mater. Chem. Phys. 118 (2009) 174-180.

[12] J. Wang, F. Ren, R. Yi, A. Yan, G. Qiu, X. Liu, Solvothermal synthesis and magnetic properties of size-controlled nickel ferrite nanoparticles, J. Alloys Compds. 479 (2009) 791-796.

[13] Manoj M. Kothawale, R. B. Tangsali, G. K. Naik and J. S. Budkuley, Characterization and Magnetic Properties of Nanoparticle $Ni_{1-x}Zn_xFe_2O_4$ Ferrites Prepared Using Microwave Assisted Combustion Method, J. Supercond. Nov. Magn. 25 (2012) 1907-1911.

[14] S. Mirzaee, Y.A. Kalandaragh, P. Rahimzadeh, Modified co-precipitation process effects on the structural and magnetic properties of Mn- doped nickel ferrite nanoparticles, Solid State Sci. 99 (2020) 106052 (1-6).

[15] G. Nabiyouni, M. Jafari Fesharaki, M. Mozafari and J. Amighian, Characterization and Magnetic Properties of Nickel Ferrite Nanoparticles Prepared by Ball Milling Technique, Chinese Phys. Lett. 27 (2010) 12.

[16] A. Manikandan, R. Sridhar, S. Arul Antony, S. Ramakrishna, A simple aloe vera plant-extracted microwave and conventional combustion synthesis: Morphological, optical and catalytic properties of magnetic $CoFe_2O_4$ nanostructures, J. Mol. Struct. 1076 (2014) 188-200.

[17] A. Manikandan, M. Durka, M. A. Selvi, S. Arul Antony, Sesamum indicum plant extracted microwave combustion synthesis and opto-magnetic properties of spinel $Mn_xCo_{1-x}Al_2O_4$ nano-catalysts, J. Nanosci. Nanotech. 16 (2016) 448-456.

[18] A. Manikandan, M. Durka, S. Arul Antony, Hibiscus rosa-sinensis leaf extracted green methods, magneto-optical and catalytic properties of spinel $CuFe_2O_4$ nano- and microstructures, J. Inorg. Organomet. Polym. 15 (2015) 1019–1031.

[19] A. Manikandan, M. Durka, M. A. Selvi, S. Arul Antony, Aloe vera plant extracted green synthesis, structural and opto-magnetic characterizations of spinel $Co_xZn_{1-x}Al_2O_4$ nano-catalysts, J. Nanosci. Nanotech. 16 (2016) 357-373.

[20] P. Bhavani, A. Manikandan, P. Paulraj, A. Dinesh, M. Durka, and S. Arul Antony, Okra (Abelmoschus esculentus) Plant Extract-Assisted Combustion Synthesis and Characterization Studies of Spinel $ZnAl_2O_4$ Nano-Catalysts, J. Nanosci. Nanotech. 18 (2018) 4072–4081.

[21] N. Babitha, L. Srimathi Priya, S. Rosy Christy, A. Manikandan, A. Dinesh, M. Durka, and S. Arunadevi, Enhanced Antibacterial Activity and Photo-Catalytic Properties of ZnO

Nanoparticles: Pedalium Murex Plant Extract-Assisted Synthesis, J. Nanosci. Nanotech. 19 (2019) 2888–2894.

[22] C. Ragupathi, J. Judith Vijaya, A. Manikandan, L. John Kennedy, Phytosynthesis of nano $ZnAl_2O_4$ by using sesamum (sesamum indicum L.); optical and catalytic properties, J. Nanosci. Nanotech. 13 (2013) 8292-8306.

[23] S. Moortheswaran, A. Manikandan, S. Sujatha, S. K. Jaganathan, S. Arul Antony, Selective catalytic oxidation of benzyl alcohol and characterization studies of spinel $MnAl_2O_4$ nanoparticles by a facile synthesis route, Nanosci. Nanotechnol. Lett. 8 (2016) 434-437.

[24] S.K. Gore, S.S. Jadhav, U.B. Tumberphale, S.M. Shaikh, M. Naushad, R.S. Mane, Cation distribution, magnetic properties and cubic-perovskite phase transition in bismuth-doped nickel ferrite, Solid State Sci.74 (2017) 88-94.

[25] S.U. Bhaskera, Y. Veeraswamy , N. Jayababu , M.V. Ramanareddy, Chromium substitution effect on the structural, optical, electrical and magnetic properties of Nickel ferrite nano particles; synthesized by an environmentally benign auto combustion method, Mater. Today: Proceedings 3 (2016) 3666-3672.

[26] J. Wanga, F. Ren, R. Yi, A. Yan, G. Qiu, X. Liu, Solvothermal synthesis and magnetic properties of size-controlled nickel ferrite nanoparticles, J. Alloys Compd. 479 (2009) 791–796.

[27] S Asiri, Murat Sertkol, S Guner, H Gungunes, KM Batoo, Tawfik A Saleh, H Sozeri, Munirah Abdullah Almessiere, A Manikandan, Abdulhadi Baykal, Hydrothermal synthesis of $Co_yZn_yMn_{1-2y}Fe_2O_4$ nanoferrites: magneto-optical investigation, Ceram. Int. 44 (2018) 5751-5759.

[28] NA Algarou, Y Slimani, MA Almessiere, A Baykal, S Guner, A Manikandan, I Ercan, Enhancement on the exchange coupling behavior of $SrCo_{0.02}Zr_{0.02}Fe_{11.96}O_{19}/MFe_2O_4$ (M= Co, Ni, Cu, Mn and Zn) as hard/soft magnetic nanocomposites, J. Magn. Magn. Mater. 499 (2020) 166308.

[29] MA Almessiere, E Hannachi, Y Slimani, Ghulam Yasin, M Mumtaz, MR Koblischka, A Koblischka-Veneva, A Manikandan, A Baykal, Dimensionality and superconducting parameters of $YBa_2Cu_3O_{7-d}/(WO_3$ $NPs)_x$ composites deduced from excess conductivity analysis, Mater. Chem. Phys. 243 (2020) 122665.

[30] MA Almessiere, Y Slimani, H Gungunes, M Nawaz, FS Al-ahmari, A Manikandan, A Baykal, Investigation of the crystal/magnetic structure, magnetic and optical properties of $SrY_xNb_xFe_{12-2x}O_{19}$ ($x \le 0.05$) hexaferrites, Phys. Scripta 95 (2020) 055802.

[31] C. Singh, A. Goyal and S. Singhal, Nickel-doped cobalt ferrite nanoparticles: efficient catalysts for the reduction of nitroaromatic compounds and photo-oxidative degradation of toxic dyes, DOI: 10.1039/c4nr01730g.

[32] A. Naduman, K. Shetty, K.S. Anantharaju, H.P. Nagaswarupa, D. Rangappa, Y.S. Vidya, H. Nagabhushana, S.C. Prashantha, Sunlight photocatalytic performance of Mg-doped nickel ferrite synthesized by a green sol-gel route, J. Sci.: Advan. Mater. Devices 4 (2019) 89-100.

[33] Hirthna, S. Sendhilnathan, Enhancement in dielectric and magnetic properties of Mg^{2+} substituted highly porous super paramagnetic nickel ferrite nanoparticles with Williamson-Hall plots mechanistic view, Ceram. Int. 43 (2017) 15447-15453.

[34] P Thilagavathi, A Manikandan, S Sujatha, SK Jaganathan, S Arul Antony, Sol–gel synthesis and characterization studies of $NiMoO_4$ nanostructures for photocatalytic degradation of methylene blue dye, Nanosci. Nanotechnol. Lett. 8 (2016) 438-443.

[35] C.Y. Zhang, X.Q. Shen, J.X. Zhou, M.X. Jing, K. Cao, Synthesis and magnetic properties of nanocomposite $Ni_{1−x}Co_xFe_2O_4$–$BaTiO_3$ fibers by organic gel-thermal decomposition process, J. Sol-Gel Sci. Technol. 42 (2007) 95.

[36] S. Maensiri, C. Masingboon, B. Boonchom and S. Seraphin, A simple route to synthesize nickel ferrite ($NiFe_2O_4$) nanoparticles using egg white, Scripta Materialia 56 (2007) 797-800.

[37] Y Slimani, MA Almessiere, E Hannachi, A Baykal, A Manikandan, M Mumtaz, F Ben Azzouz, Influence of WO_3 nanowires on structural, morphological and flux pinning ability of YBa_2Cu_3Oy superconductor, Ceram. Int. 45 (2019) 2621-2628.

[38] V. Umapathy, A. Manikandan, S. Arul Antony, P. Ramu, P. Neeraja, Synthesis, structural, morphological and opto-magnetic properties of Bi_2MoO_6 nano-photocatalyst by sol-gel method, Trans. Nonferrous Met. Soc. China 25 (2015) 3271-3278.

[39] A. Manikandan, S. Arul Antony, A novel approach for the synthesis and characterization studies of Mn^{2+} doped CdS nano-crystals by a facile microwave combustion method, J. Supercond. Nov. Magn. 27 (2014) 2725-2733.

[40] S. Jayasree, A. Manikandan, A. M. Uduman Mohideen, C. Barathiraja, S. Arul Antony, Comparative study of combustion methods, opto-magnetic and catalytic properties of spinel $CoAl_2O_4$ nano- and microstructures, Adv. Sci., Eng. Med. 7 (2015) 672-682.

[41] A. Manikandan, L. John Kennedy, J. Judith Vijaya, Structural, optical and magnetic properties of porous α-Fe_2O_3 nanostructures prepared by rapid combustion method, J. Nanosci. Nanotech. 13 (2013) 2986-2992.

[42] S. Asiri, M. Sertkol, H. Gungunes, Md Amir, A. Manikandan, I. Ercan, A. Baykal, The temperature effect on magnetic properties of $NiFe_2O_4$ nanoparticles, J. Inorg. Organomet. Polym. 28 (2018) 1587–1597.

[43]. A. Muthukrishnaraj, A. Arun, S. S. Kalaivani, T. Maiyalagan, A. Manikandan, N. Balasubramanian, Solvothermal synthesis and characterizations of graphene-$ZnBi_{12}O_{20}$ nanocomposites for visible-light driven photocatalytic applications, Ceram. Int. 46 (2020) 18534-18543.

[44] R. A. Senthil, S. Osman, J. Pan, Y. Sun, T. R. Kumar, A. Manikandan, A facile hydrothermal synthesis of visible-light responsive $BiFeWO_6$/MoS_2 composite as superior photocatalyst for degradation of organic pollutants, Ceram. Int. 45 (2019) 18683-18690.

[45] A Muthukrishnaraj, SS Kalaivani, A Manikandan, Helen P Kavitha, R Srinivasan, N Balasubramanian, Sonochemical synthesis and visible light induced photocatalytic property of reduced graphene oxide@ ZnO hexagonal hollow rod nanocomposite, J. Alloys Compd. 83625 (2020) 155377.

[46] R. A. Senthil, S. Osman, J. Pan, A. Khan, V. Yang, T. R. Kumar, Y. Sun, A. Manikandan, One-pot preparation of AgBr/α-Ag_2WO_4 composites with superior photocatalytic activity under visible-light irradiation, Colloids Surf. A: Physicochem. Eng. Aspects 586 (2020) 124079.

[47] R. Bomila, S. Srinivasan, S. Gunasekaran, A. Manikandan, Enhanced photocatalytic degradation of methylene blue dye, opto-magnetic and antibacterial behaviour of pure and La-doped ZnO nanoparticles, J. Supercond. Nov. Magn. 31 (2018) 855–864.

[48] K. Chitra, K. Reena, A. Manikandan, S. Arul Antony, Antibacterial studies and effect of poloxamer on gold nanoparticles by Zingiber officinale extracted green synthesis, J. Nanosci. Nanotech. 15 (2015) 4984-4991.

[49] K. Chitra, A. Manikandan, S. Moortheswaran, K. Reena, S. Arul Antony, Zingiber officinale extracted green synthesis of copper nanoparticles: Structural, morphological and antibacterial studies, Adv. Sci. Eng. Med. 7 (2015) 710-716.

[50] K. Chitra, A. Manikandan, S. Arul Antony, Effect of poloxamer on Zingiber officinale extracted green synthesis and antibacterial studies of silver nanoparticles, J. Nanosci. Nanotech. 16 (2016) 758-764.

[51] A Manikandan, E Manikandan, B Meenatchi, S Vadivel, SK Jaganathan, Rare earth element (REE) lanthanum doped zinc oxide (La: ZnO) nanomaterials: synthesis structural optical and antibacterial studies, J. Alloys Compd.723 (2017) 1155-1161.

[52] V. Sumithra, A. Manikandan, M. Durka, S. K. Jaganathan, A. Dinesh, N. Ramalakshmi, S. Arul Antony, Simple precipitation synthesis, characterization and antibacterial activity of Mn-doped ZnO nanoparticles, Adv. Sci. Eng. Med. 9 (2017) 483–488.